https://doi.org/10.1016/j.compgeo.2020.103974

An enhanced tool for probing the microscopic behavior of granular materials based on X-ray micro-CT and FDEM

Yuan Chen[a,b,c], Gang Ma[a,c,*], Wei Zhou[a,c], Deheng Wei [d], Qi Zhao [e], Yuxiong Zou[a,c], Giovanni Grasselli[f]

[a] State Key Laboratory of Water Resources and Hydropower Engineering Science, Wuhan University, Wuhan 430072, China
[b] Changjiang Survey, Planning, Design and Research Co., Ltd., Wuhan 430010, China
[c] Key Laboratory of Rock Mechanics in Hydraulic Structural Engineering of Ministry of Education, Wuhan University, Wuhan 430072, China
[d] School of Civil Engineering, the University of Sydney, Sydney, Australia
[e] Department of Civil and Environmental Engineering, the Hong Kong Polytechnic University, Hung Hom, Kowloon, Hong Kong, China
[f] Department of Civil and Mineral Engineering University of Toronto, 35 St George St., Toronto, ON M5S 1A4, Canada

Corresponding author: Gang Ma (magang630@whu.edu.cn)

Abstract: We propose an enhanced tool by combining X-ray micro-computed tomography test and hybrid finite and discrete element method to investigate the mechanical behaviors of granular materials. We first conduct a min-triaxial test of Ottawa sand under X-ray micro-CT. Then, spherical harmonic analysis is performed to characterize multi-scale morphological characteristics of particles and used in the particle matching. The particle tracking algorithm ensures the matching accuracy between particle configurations even at large strain intervals. To probe intra-particle contact force, we reconstruct the numerical sample from X-ray image data. Without calibrating material parameters, FDEM simulation quantitatively agrees with the overall response of Ottawa sand recorded in experiment. Moreover, the particle scale dynamics obtained by simulation are remarkably quantitatively consistent with experiment results. The proposed tool sheds new light on bridging length scales from

particle to granular system. We find that the granular material deforms plastically through spatially localized zones of large nonaffine displacements, and the spatiotemporal evolution of these zones controls the macroscopic responses of the system. The force chain collapse is relevant to the large induced structural voids formation within the shear transformation zones. Furthermore, we discover a connection between particle stress fluctuations and particle plastic rearrangements in granular materials.

Keywords: Granular materials; X-ray micro-computed tomography; FDEM; Particle matching and tracking; Microscopic dynamics; Intra-particle contact force

1. Introduction

Granular materials, especially consist of naturally occurring geo-materials and fault gouge, deform and failure in response to external mechanical loading, such as natural landslides, soil foundation instability, avalanches. Because of the inherently amorphous nature in granular system, the microstructure of confined granular materials is heterogenous and disordered. The granular system responds to the mechanical stimuli through the spatial rearrangement of particles and the dynamics of force transmission network [1]. Therefore, the measurements of particle motion and the intra-particle force transmission are significant to understand the underlying physics and mechanisms responsible for the loss of structural stability.

More recently, advanced tomographic techniques, such as X-ray computed tomography [2-7], 3D X-ray diffraction microscopy [8,9], have been successfully used to characterize the structural properties and particle scale dynamics throughout the full 3D systems. X-ray computed tomography aided laboratory test allows for the investigation of granular materials from micro-meso-macro perspectives [10-17], thus

making it a promising tool in studying the complex granular systems. Tracking the trajectory of large number of moving particles remains a challenge, especially for the granular system undergoing large deformation and the large scanning interval. Andò et al. [2] first developed a particle matching algorithm using particle volume as matching index to identify the same particle between adjacent assembly configurations. Subsequently, more morphological features are used in particle matching and tracking algorithm [18], such as the particle volume, surface area, and principal axis lengths of the particle. These morphological quantities are fairly sensitive to the X-ray CT images processing precision. One promising way of improving the matching accuracy is to use more morphological features ranging from particulate size to surface texture. Spherical harmonic (SH) analysis is capable of characterizing and quantifying the multiscale morphological features of irregular shaped particles [19-22]. The SH invariants, independent of particle translation and rotation, are adopted in evaluating the similarities of particles and thus can help to track particles across multiple loading frames [23-25].

Although having the tremendous ability in exploring the dynamics of granular system, X-ray CT techniques lack the ability of probing intra-particle contact behaviors. Saadatfar et al. [26] measure contact forces from X-ray CT data, but this work is restricted to spherical particles and highly depends on the assumption of Hertzian contact behavior. By combining the Granular Element Method (GEM) and X-ray CT data, Andrade and Hurley [27,28] infer the local contact forces by inversely solving the governing equations of granular materials in static equilibrium. However, this method is computationally expensive and thus limited to a small granular system. Recently, Hurley et al. [29] develop a new technique by combining the X-ray tomography and X-ray diffraction, which allows for the quantitative measurements of

microscopic structure [9], intra-particle forces [30,31], and energy dissipation due to grain fracture [32,33]. These investigations are carried out in single-crystal granular systems with a limited number of particles as several hundred. The particle based numerical simulation methods are versatile in direct probing the intra-particle force transmission in large-scale granular system [34,35]. The commonly accepted idea that particle shape has profound influences on granular dynamic behavior promotes the development of more advanced modeling techniques [7][36], such as the combined finite and discrete element method (FDEM) [37-39], DEM [67] and the LS-DEM method [40,41]. The studies proposed by researchers [41][67] shows great effectiveness in considering the irregular particle shapes. FDEM has great advantages not only in considering the irregular particle shapes but also in particle breakage [42-49]. In FDEM analysis framework, each individual particle with arbitrary shape is discretized into finite element meshes, and the particle-level stress and strain field and contact force are governed by the material constitutive law and penalty contact algorithm, respectively.

Arising from the limitations in pure experimental test and numerical simulation, the present work develops an enhanced tool for probing the microscopic behavior of granular materials by combining X-ray micro-CT test and FDEM modeling. The schematic illustrations of the present work is shown in Fig. 1. A mini-triaxial shear test of Ottawa sand is first carried out under X-ray micro-CT. Spherical harmonic analysis is then performed to characterize the particle shape and track moved particles during the loading process. We prepare the numerical sample for FDEM simulation with the spherical harmonic mathematical reconstruction of particle shape. Quantitative comparison and investigation of macroscopic responses and microscopic

dynamics in FDEM simulation and X-ray micro-CT test are performed. Then the plastic behaviors of the sheared granular system are discussed. The contact force evolution is further assessed through FDEM simulation to gain in-depth understanding of the mechanism responsible for the failure of sheared granular system.

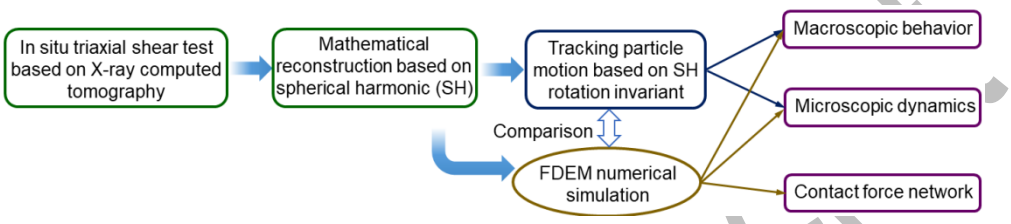

Fig.1. Schematic description of the present research.

2. Experiments of triaxial test based on X-ray computed tomography

2.1 Experimental method

In the present work, experiment tests are carried out using the ERDμ apparatus [50,51] to subject the Ottawa sand sample to shear condition (Figs. 2a and 2b). The diameter of the tested Ottawa sand grain ranges from 0.3 to 1.03 mm with a mean particle diameter of 0.551 mm (Fig. 2c). The cylindrical sample is prepared by dry pluviation method and subjected to vibration and tap horizontally and vertically until attaining a dense packing [52], with an initial diameter of approximately 12 mm and a height of 25 mm. The test sample is confined by a 0.3 mm thick flexible latex membrane, providing the flexible boundary condition. Subsequently, the sample is placed inside the ERDμ apparatus that is mounted on the computer numerical control (CNC) rotation table inside the X-ray micro-CT [50]. The specimen sample is first isotropically compressed to 300 kPa and then subjected to strain-controlled axial loading by the downward movement of the top platen at a constant strain rate of

0.1%/min, which is small enough to ensure quasi-static condition (Fig. 2b). During experiment, tomography images of the sample are acquired nondestructively at 15 loading frames. The first scanning point is at the end of compression prior to axial loading. At each imaging stage, a total of 1080 projections with a pixel size of 27.5μm are taken by rotating the ERDμ apparatus 360° around the vertical axis, while keeping the piston stationary and confining pressure constant, which provides enough image quality for quantitative analysis of internal structure and distributions of all particles.

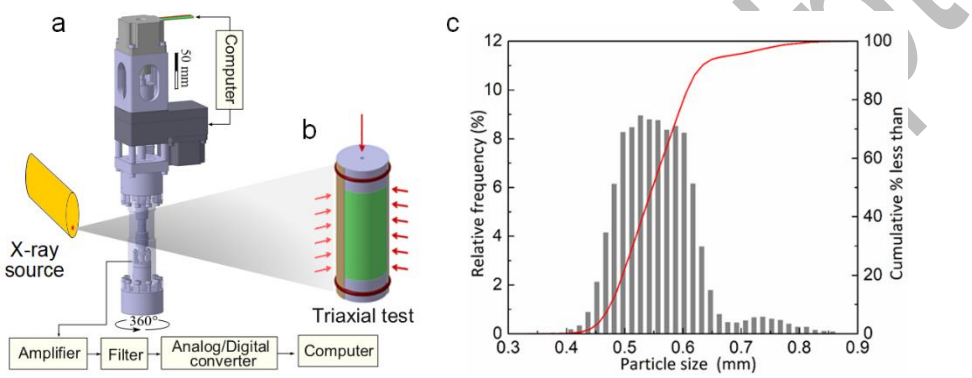

Fig. 2. Schematic diagram of the experiment setup. (a) The ERDμ vessel. (b) The sample during the experiment test. (c) Particle size distribution of Ottawa sand tested.

2.2 Image processing

The three-dimensional structure is first reconstructed based on the filtered back-projection algorithm. Then the reconstructed 3D grayscale image is transformed to a binary image and eventually to a segmentation image (Fig. 3(a)). The marker-based watershed technique [3][53,54] is used to separate particles so that each particle can be identified and labelled. In this process, a global threshold is applied to the image segmentation, which may lead to an over-estimation of inter-particle contacts because of the partial volume effect of the CT image. However, it may not influence much the overall contact behavior [15]. Following the image segmentation, 15961 individual particles are identified and automatically isolated in the test sample

(Fig. 3(b)). Voxels representing contacts between neighboring particles can be identified by subtracting the labelled data from the binary data without watershed segmentation [55]. It is noted that contact between two particles is not always a single continuous region. For particles with complex irregular morphology, several contact regions are assigned to the same contact particle pair. For this case, these isolated regions are regarded as one contact in this study, which is similar to the study of some researches [15][68]. In addition, a contact size threshold of one voxel is considered in contact detection. Those contacts with a size larger than the threshold are regarded as true contacts. The particle IDs involved in each true contact are determined via analysis of the boundary shells of each contact based on the 26 neighborhood situations consist of six faces, eight corners and twelve edges [47][55]. Therefore, the branch vectors can be clearly defined by connecting the centroids of the contact particle pairs. The contact normal vectors are determined by principal component analysis (PCA) of contact voxels [47,48].

As we have known the volume occupied by the particle voxels, we can calculate the void ratio of the sample at the beginning of axial loading, which is 0.593. The labelled data of particle assembly is then exported to MATLAB [56] as a 3D matrix for post-processing. Such a large database offers rich particle informatics.

Particle matching is a key process in tracking the trajectory of large number of moving particles across multiple loading frames. For granular system undergoing large deformation, accurate particle matching is necessary for quantifying particle kinematics. Morphological features as the intrinsic characteristics can be used in the particle matching. The spherical harmonic (SH) analysis is utilized to characterize and

quantify the multiscale morphological features of particles [19-22]. The surfaces of particles extracted from image data can be depicted via SH function:

$$r(\theta,\varphi)=\sum_{n=0}^{\infty}\sum_{m=-n}^{n}c_n^m Y_n^m(\theta,\varphi) \tag{1}$$

$$Y_n^m(\theta,\varphi)=\sqrt{\frac{(2n+1)(n-m)!}{4\pi(n+m)!}}P_n^m(\cos\theta)e^{im\varphi} \tag{2}$$

where $r(\theta,\varphi)=\sqrt{\sum_{x,y,z}(\kappa-\kappa_0)^2}$ is the polar radius from particle centroid (x_0, y_0, z_0) with the pair of spherical coordinates $\theta\in[0,\pi]$ and $\varphi\in[0,2\pi]$. c_n^m is the corresponding SH coefficient, and according to Eq. (1), a total number of $(n+1)^2$ unknown coefficients need to be determined. Taking $r(\theta,\varphi)$ as the input on the left side of Eq. (1), a linear equation system with $(n+1)^2$ unknowns can be obtained. Thus it is easy to solve these linear equations and determine all of the coefficients of c_n^m by performing the standard least squares estimation for Eq. (1). $P_n^m(\cos\theta)$ denotes the Legendre function of degree n and order m, expressed by Rodrigues's formula

$$P_n^m(x)=(1-x^2)^{|m|/2}\cdot\frac{d^{|m|}}{dx^{|m|}}\left[\frac{1}{2^n n!}\cdot\frac{d^n}{dx^n}(x^2-1)^n\right] \tag{3}$$

The SH coefficients describe the general conformation of the particle shape at different scales. The more SH coefficients we use, the more detailed characterization and more accurate reconstruction of the particle shape can be achieved. It has been found that the SH analysis with spherical harmonic degree $n\geq 15$ is enough to describe the morphology of a particle (as shown in Fig. 3(b)) [57]. We can then define a set of SH frequencies as $R_n(\theta,\varphi)=\sum_{m=-n}^{n}c_n^m Y_n^m(\theta,\varphi)$, which exhibit rotational invariant properties independent of particle translation and rotation [23]. The modulus of the

SH frequency is referred to as 'SH rotation-invariant' and calculated as:

$$\left\|R_n(\theta,\varphi)\right\| = \sqrt{\int_0^{2\pi}\int_0^{\pi} R_n(\theta,\varphi)^2\, d\theta d\varphi} = \sqrt{\sum_{m=-n}^{n}\left\|c_n^m\right\|^2} \tag{4}$$

When SH degree n goes to infinity, the spherical harmonic function describes all the features it contains at different frequencies over the space of all transformations. For a particular kind of natural sand, there are no two particulates with completely identical morphology features. Consequently, any natural sand of such kind has a unique set of SH rotation-invariants depicting its collective morphological features over full SH degree. Therefore, the SH rotation-invariants can be used as the geometrical DNA for matching particle. SH function, approximating particle morphology in collective derivations of polar radius via different SH degrees, is band-limited with a bandwidth, hence information loss may happen when SH function goes to its SH rotation-invariants, because the spatial dimension changes. This phenomenon generally happens in the case where the bandwidth is too small to describe the multiscale morphology of natural sand. In this study, the maximum of SH degree is set to 15, and the SH rotation-invariants are sufficient to represent the morphological features at multi-scales, i.e., R_0 represents the particle volume, R_2 to R_4 represent the general shape, R_5 to R_8 represent the local roundness, and R_9 to R_{15} represent the surface texture at very small scale level [57]. The correlation coefficient matrix shown in Fig. 4 demonstrates that the SH rotation-invariants are relatively independent of each other, especially between different scales. Thus, we can conclude that particle shape characterization using SH rotation-invariants is comprehensive. Hence, we can identify the matching particles between adjacent loading frames by evaluating the minimum $L^2\text{-}norm$ difference between the corresponding vectors $\mathbf{R}_n$ (Fig. 3(c-d)) [25], measured by

$$\left\| R_n^k(\theta,\varphi) - R_n^{k+1}(\theta,\varphi) \right\| = \sqrt{\sum_{n=0}^{\infty} \left(\left\| R_n^k \right\| - \left\| R_n^{k+1} \right\| \right)^2} \quad (k = 1, 2, \mathrm{K}, N_S) \tag{5}$$

where k is the loading states and N_S is the total number of micro-CT scan points.

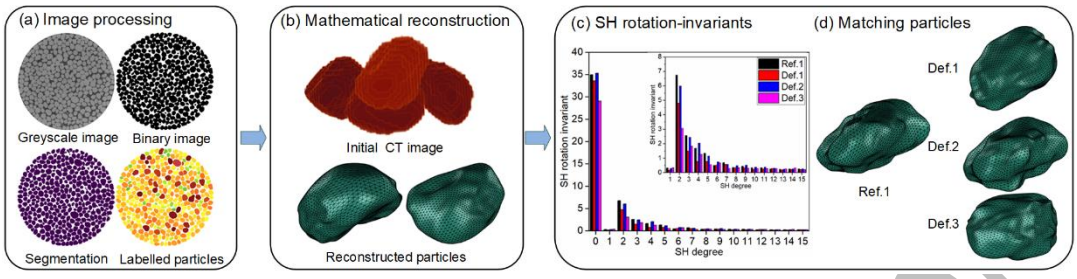

Fig. 3. Schematic flow of the 3-dimensional image processing and modeling. (a) Processing of 3D image segmentation. (b) Mathematical characterization and modeling of particle surface based on spherical harmonic reconstruction. (c) Statistical difference of derived spherical harmonic rotation-invariants at different SH-degrees (one particle is from reference (Ref.) configuration and three particles are from deformed (Def.) configuration). (d) Digital reconstruction of particles selected and matching results (particle Ref.1 matches to particle Def.2).

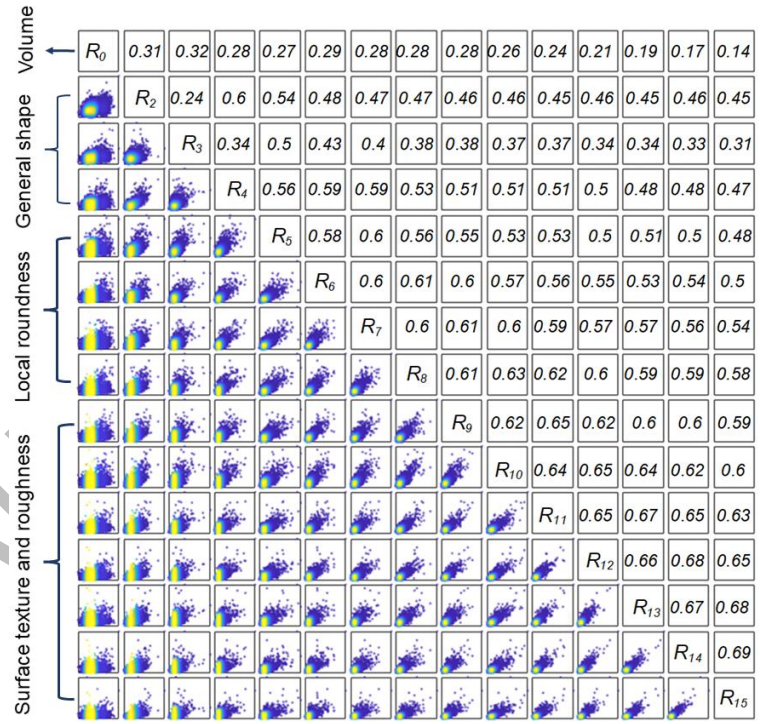

Fig. 4. Correlation coefficient matrix of the SH rotation-invariants for all particles in sample. The color represents the data point density in range (0, 1) and the yellow represents the higher density.

As shown in **Algorithm 1**, a pseudo-code representation of particle matching and tracking algorithm, we first construct a superset of candidate particles by evaluating

the particle distance between two successive loading frames. The particles within $3d_{50}$ of particle i are selected and denoted as ${}^{1}\mathbf{C}^{k,i}$. We then narrow the superset by removing the particles with volume difference larger than 10% of particle i. We therefore obtain the superset ${}^{2}\mathbf{C}^{k,i}$ with those remaining particles j. Note that, if ${}^{2}\mathbf{C}^{k,i}$ is an empty set, we specify the reference particle i is lost [2][14]. Among them, the one that corresponds to the minimum $L_2\text{-}norm$ difference $\mathbf{R_D}^{k,i}$ of spherical harmonic rotational invariants between particle i is temporarily identified as the matching particle and stored into subset ${}^{3}\mathbf{C}^{k,i}$. If a particle is found to be assigned in more than one reference particles' subsets, the reference particle with the smallest $\mathbf{R_D}^{k,i}(j)$ is considered as the best match. Subsequently, the other reference particle rematches again after the candidate particle is removed from its subset. We repeat this matching process for particles in reference configuration and finally determine a matching set $\mathbf{T}^{k}$. During each matching regime, just a few dozen particles are lost or incorrectly matched, which is induced by information loss or image segmentation error, such as over-segmentation and under-segmentation. Overall, the matching provides highly accurate matching results. Due to the limited contents of this study, the detailed description of the tracking efficiency is illustrated in Appendix A.

Algorithm 1. Particle matching based on spherical harmonic rotational invariant

Require: Spherical harmonic rotational invariant vector $\mathbf{R}^{k,i}$, $\mathbf{R}^{k+1,j}$, particle's centroid $\mathbf{r}^{k,i}$, $\mathbf{r}^{k+1,j}$ and volume $v^{k,i}$, $v^{k+1,j}$ of particle i at loading state k and particle j at loading state $k+1$ by evaluating eq.(4); Average particle diameter d_{50}, total number N of particles.

1: $\mathbf{R}^{k,i} \leftarrow \left\{\left\|R_0^{k,i}(\theta,\varphi)\right\|, \left\|R_1^{k,i}(\theta,\varphi)\right\|, \mathrm{K}, \left\|R_n^{k,i}(\theta,\varphi)\right\|\right\}$

2: $\mathbf{R}^{k+1,j} \leftarrow \left\{\left\|R_0^{k+1,j}(\theta,\varphi)\right\|, \left\|R_1^{k+1,j}(\theta,\varphi)\right\|, \mathrm{K}, \left\|R_n^{k+1,j}(\theta,\varphi)\right\|\right\}$

3: **for** $i = 1$ to *Number of particles* in reference configuration **do**

4: / * Search particles j locating in the certain region from particle i * /

5: **for** $j = 1$ to *Number of particles* in deformed configuration **do**

if L_2-*norm* $(\mathbf{r}^{k+1,j} - \mathbf{r}^{k,i}) \leq 3d_{50}$ **then**
  ${}^{1}\mathbf{C}^{k,i} \leftarrow \{j\}$
end if
end for
/* Update matching array by estimating the volume difference tolerance */
for particle j is in the first matching set $\{{}^{1}\mathbf{C}^{k,i}\}$ **do**
if $\left|v^{k+1,j} - v^{k,i}\right| / v^{k,i} \leq 0.1$ **then**
  ${}^{2}\mathbf{C}^{k,i} \leftarrow \{j\}$
  $\mathbf{R_D}^{k,i} \leftarrow$ L_2-*norm* $(\mathbf{R}^{k+1,j} - \mathbf{R}^{k,i})$
end if
end for
$m \leftarrow 1;\ l \leftarrow i$
while $m \geq 1$ **do**
if $\mathbf{R_D}^{k,l}$ is an empty set **then**
  $m \leftarrow -1;\ {}^{3}\mathbf{C}^{k,l} \leftarrow 0$
else
  ${}^{3}\mathbf{C}^{k,l} \leftarrow j$ corresponding to $\min(\mathbf{R_D}^{k,l})$
  /* Judge if j has been matched to previous particle p, and confirm which particle is more similar to particle j */
if ${}^{3}\mathbf{C}^{k,l} = {}^{3}\mathbf{C}^{k,p}$ and $\mathbf{R_D}^{k,p}(j) \leq \mathbf{R_D}^{k,l}(j)$ **then**
  $m \leftarrow m+1$
  remove $\mathbf{R_D}^{k,l}(j)$ from L_2-*norm* difference vector $\mathbf{R_D}^{k,l}$
end if
if ${}^{3}\mathbf{C}^{k,l} = {}^{3}\mathbf{C}^{k,p}$ and $\mathbf{R_D}^{k,p}(j) > \mathbf{R_D}^{k,l}(j)$ **then**
  $m \leftarrow m+1$
  remove $\mathbf{R_D}^{k,p}(j)$ from L_2-*norm* difference vector $\mathbf{R_D}^{k,p}$; $l \leftarrow p$
end if
  $m \leftarrow m-1$
end if
end while
$\mathbf{T}^{k} \leftarrow \{{}^{3}\mathbf{C}^{k,i}\}$
end for
Return $\{\mathbf{T}^{k}\}$

3. Numerical modeling based on FDEM

3.1 Numerical framework and model formulation

Strictly speaking, the FDEM technique alternates between employing FEM formulation to assess the deformation and stress in individual particle level and DEM concepts for handling contact detection and contact interaction between discrete

particles. The dynamic equation of FDEM is essentially the same as that of DEM. That is, the dynamic equation of the element nodes is expressed by Newton's second law as:

$$\mathbf{M}\ddot{\mathbf{u}} + \mathbf{C}\dot{\mathbf{u}} = \mathbf{F}_{\mathbf{ext}} + \mathbf{F}_{\mathbf{con}} - \mathbf{F}_{\mathrm{int}} \tag{6}$$

where $\ddot{\mathbf{u}}$ and $\dot{\mathbf{u}}$ are acceleration and velocity vectors of nodes, respectively; $\mathbf{M}$ and $\mathbf{C}$ are the lumped mass matrix and damping matrix of nodes, respectively; $\mathbf{F}_{\mathrm{int}}$, $\mathbf{F}_{\mathbf{ext}}$, and $\mathbf{F}_{\mathbf{con}}$ is the nodal force vector caused by the deformation of elements, by the external load distributed to the node and by the contact force, respectively. The solution of Eq. (6) uses the same method as the DEM, namely, that the dynamic equation of element nodes is integrated using the explicit central-difference integration scheme. In FDEM approach, the contact mechanics is solved by a distributed contact force approach applied to element nodes and a penalty function method. Viscous damping is introduced to maintain the numerical stability and the quasi-static equilibrium. Thus, combining the elastic and viscous contributions, the distributed normal contact force is calculated as:

$$F_n = k_n \delta_n - 2\beta_n \sqrt{m k_n} v_{rn} \tag{7}$$

The tangential friction force is calculated by a Coulomb-type friction law:

$$F_t = \min\left\{ \left| \Sigma k_t \dot{\gamma} \Delta t - 2\beta_t \sqrt{m k_t} v_{rt} \right|, \mu F_n \right\} \tag{8}$$

where $k_n = p_n A_{node}$ and $k_t = p_t A_{node}$ are the contact stiffness along the normal and tangential direction at nodes, receptively; p_n (p_t) is the normal (tangential) penalty stiffness, A_{node} is the node's control area on the contacting surface, δ_n is the penetration, $\dot{\gamma}$ is the slip rate, Δt is the time increment. β_n (β_t) is the normal (tangential) critical damping fraction corresponding to a restitution coefficient ξ by

$\beta = -\ln(\xi)/\sqrt{\pi^2 + \ln^2(\xi)}$ [46]. m is the mass of node and v_{rn} (v_{rt}) is the normal (tangential) relative velocity between contact particles. Due to the Coulomb frictional limit, the total tangential force is depending on the friction coefficient m of the material.

3.2 Bridging the experimental test and numerical modeling

As a pre-processing stage, a shape library containing multi-scale morphologies of Ottawa particles, explicitly represented by the spherical harmonic analysis described above (section 2), is extracted from the X-ray micro-CT image data. The packing procedure mimics the sample preparation in laboratory, aiming to generate a numerical sample for FDEM simulation statistically consistent with the Ottawa sand tested (see Fig. 5(a-b)), such as the volume fraction, grain-size distribution, and microstructural properties. Each particle is meshed into second-order tetrahedral finite elements, as a result, millions of elements represent the sample in the numerical domain. To evaluate the similarity between numerical and experimental samples, we compare the structural properties of two samples prior to shearing. In a granular system, the pair correlation function $g(r) = n(r)/\rho 4\pi r^2 dr$ describes how density varies as a function of distance from a reference particle. It is a measure of how many particles are within a distance of r and $r + dr$ away from a particle. $n(r)$ is the number of particle within the shell, $\rho = N/V$ is the average density of particles, that is, the ratio of the total number of particles to the volume of the sample . As shown in Fig. 6a, the pair correlation functions are similar to each other and exhibit no long-range ordering and the first peak is small and broad, so that the particle assembly can be regarded as a highly disordered system. Fig. 6b shows that coordination number (CN) distributions of numerical and experimental samples are similar,

although the numerical sample keeps a relatively larger proportion of CNs around a value of 7. The angular distributions of branch vectors (see Fig. 6c) and contact normal vector (see Fig. 6d) demonstrate no significant difference, manifesting as the almost isotropic states. The statistical consistency ensures that the reconstructed numerical sample is a representative of the experiment granular system.

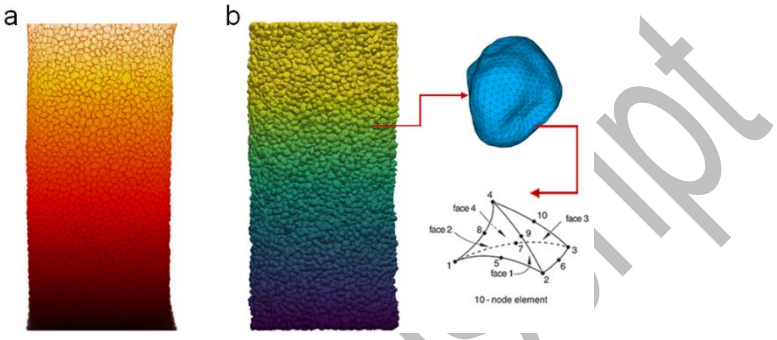

Fig. 5. Reconstruction of the Ottawa sand sample (a) 3D rendering of the X-ray tomography data for the experimental sample. (b) Numerical sample and the finite element discretization.

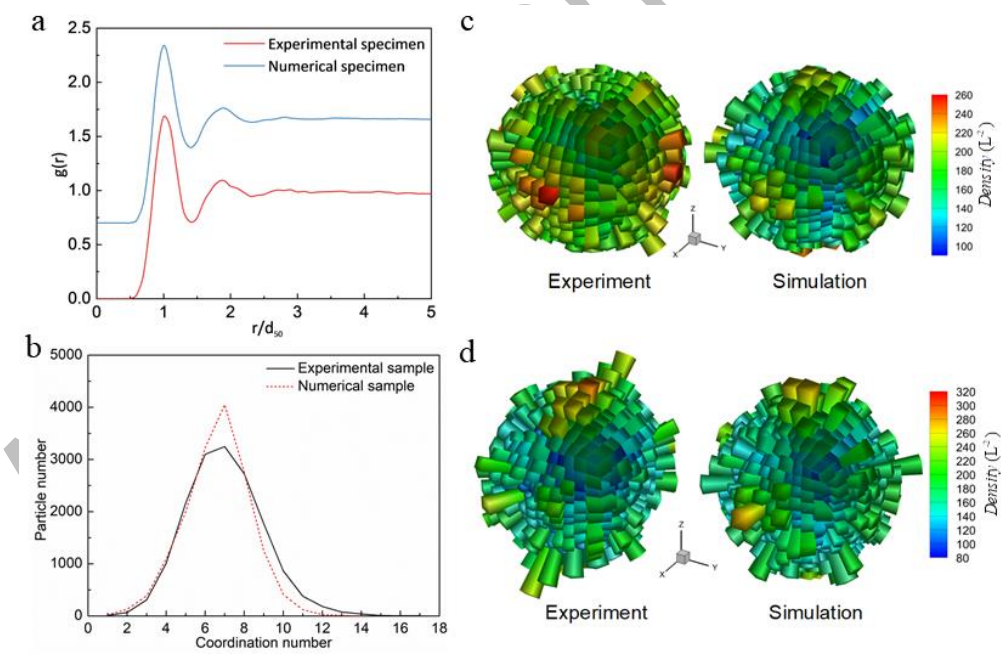

Fig. 6. Comparisons of the numerical and experimental samples. (a) The pair correlation function g(r), data for numerical sample are shifted vertically by 0.7 for clarity, (b) Distribution of the coordination number, (c-d) Angular distribution of branch vectors and contact normal vector, the length and color of each corner indicate the density of branch vector and contact normal vector oriented within the angles, respectively

We investigate the evolution of particle size distribution (PSD) in the laboratory

test of Ottawa sand (Fig. 7). The excellent agreement of PSDs reveals the fact that no significant damage to particles occurs in laboratory test. The negligible difference seen stems in part from the particle surface abrasion or segmentation precision. Therefore, there is no need to consider particle breakage in FDEM simulation. To mimic the experiment testing conditions, the numerical sample is confined by the smooth rigid platen on top and bottom as well as a thin flexible cylindrical-membrane. The membrane elements are capable of deforming flexibly to accommodate the sample deformation. The strain-controlled loading rate in FDEM simulation is several orders of magnitude larger than the experimental test to attain enough computational efficiency, but can still guarantee the quasi-static loading condition while keeping kinetic energy below 5% of internal energy. The material parameters used in the FDEM simulation are listed in Table 1, obtained from laboratory test or relevant literatures. We note that the values of Young's modulus and Poisson's ratio lie in the range of experimental measurements for Ottawa sand [58]. The normal and tangential penalty stiffnesses ensure that the contact relationship of two elastic spheres follows Hertz contact law [39]. It is worth noting that all modeling parameters except damping fractions β are consistent with experimental measurements and theory. As suggested by Tatone and Grasselli [69], when penalty terms are adopted magnitudes that are two orders of magnitude of the input elastic modulus, a reduction of time step is not necessary to maintain numerical stability. Therefore, in this work, the penalty terms p_n and p_t are set to two orders of magnitude of the input elastic modulus.

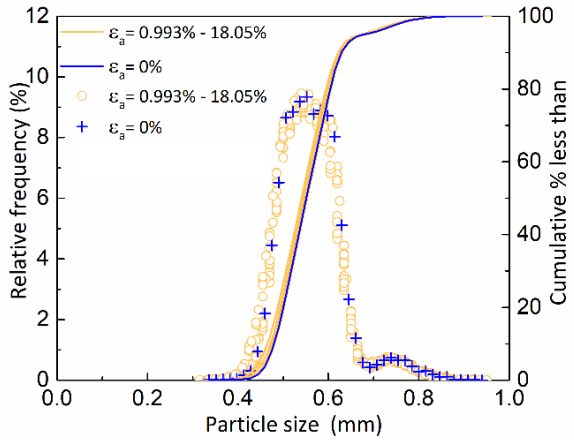

Fig. 7. Evolution of particle size distributions in experiment covering all the whole loading.

Table 1

Material parameters used in the FDEM simulation.

Parameter		Value	Unit	Reference
Density	ρ	2650	kg/m^3	[49]
Young's modulus	E	92.1	GPa	Instrumented nanoindentation
Poisson' s ratio	υ	0.118	-	[47]
Sliding friction coefficient	μ	0.5	-	[59]
Normal and Tangential penalty	p_{n} p_{t}	92.1×10^{11}	N/m^3	[69]
Critical damping fraction in normal and tangential direction	β_{n} β_{t}	0.03	-	[46]

4. Quantitative comparison between X-ray CT test and FDEM

4.1 Macroscopic behavior

We first compare the macroscopic responses obtained from experiment test and FDEM simulation. Fig.8 shows the stress-strain-dilation curves. Overall, the FDEM simulation of reconstructed Ottawa sand sample can reasonably reproduce the macroscopic behaviors recorded in experiment test. The simulation shows an earlier peak stress ratio σ_1/σ_3 from the experiment, indicating a slight difference in particle rearrangement, and that particle abrasion occurred in experiment are not considered in FDEM simulation. The overall consistency again releases an important sign, what you need in modeling of granular material are particle shape and packing properties. In total, there are 15 tomography scan points at which 3D tomography scans are taken. Note that, the drop of stress ratio during each scan point is due to the stress relaxation caused by loading pause during each X-ray imaging.

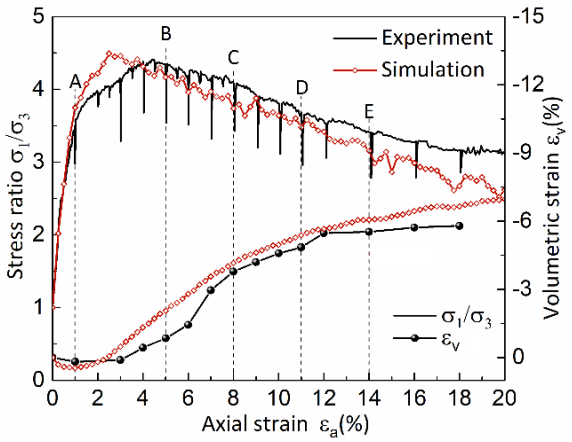

Fig. 8. Macroscopic responses obtained from the experiment test and numerical simulation. Dashed lines indicate the five strain states corresponding to the five X-ray micro-CT scan points (A to E) shown in future analysis. The negative values of volumetric strain indicate dilation.

Besides the macroscopic responses, we further compare the particle kinematics obtained from X-ray micro-CT test and FDEM simulation. For experiment test, the obtained matching set $\mathbf{T}^k$ (introduced in section 2.2) serves as bridging signal for directly tracking the kinematic of the individual particles throughout the loading process. Thus we compare the incremental particle displacements at six strain states, as marked in Fig. 9. We make the particles transparent whose displacement lies in the median domain to clearly show the internal particle displacement field. The FDEM simulated particle motion field is also in good agreement with that obtained in the X-ray micro-CT test, that is, the magnitude of particle displacement increases as the shearing process and bulging is shown in all of the snapshots. Two cone-shaped dead zones are well developed at the top and bottom of the sample at the post-peak softening stages. While in the middle of the sample, a zone of intensive shearing localizes into an X-shaped shear band, bordering on an arched motion zone distributed by the particle with low translation. We also quantitatively compare the frequency distributions of the particle displacements shown in Fig. 10(a). Overall, we see that there is a good agreement at the distributions of particle kinematics between the experiment and the FDEM simulation. It is clear in Fig. 10(b) that the particle displacements during

corresponding axial strain increments are close between experiment and simulation. These results demonstrate that the simulation quantitatively reproduces the motion behavior at the particle scale level of the experiment.

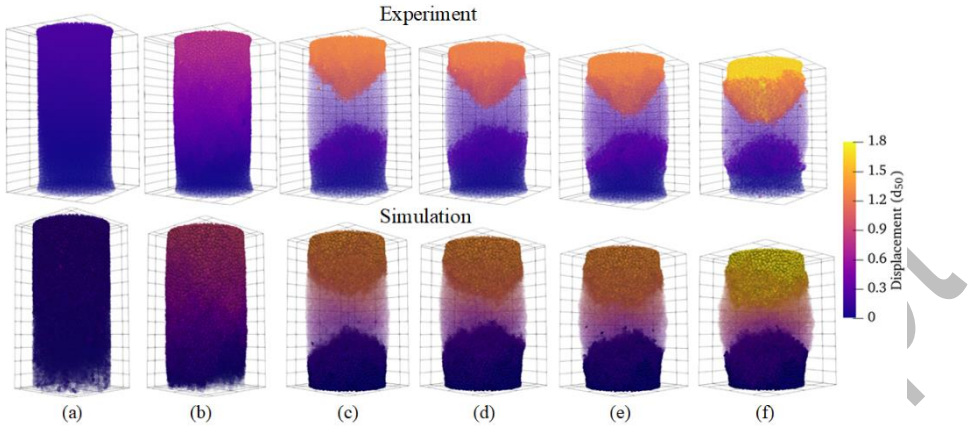

Fig. 9. Incremental particle displacements between (a) 0.0 and 0.99%, (b) 0.99 and 5.03%, (c) 5.03 and 8.06%, (d) 8.06 and 11.06%, (e) 11.06 and 14.06%, (f) 14.06 and 18.06% axial strain for experimental test and FDEM simulation. The color of particle represents the magnitude of displacement.

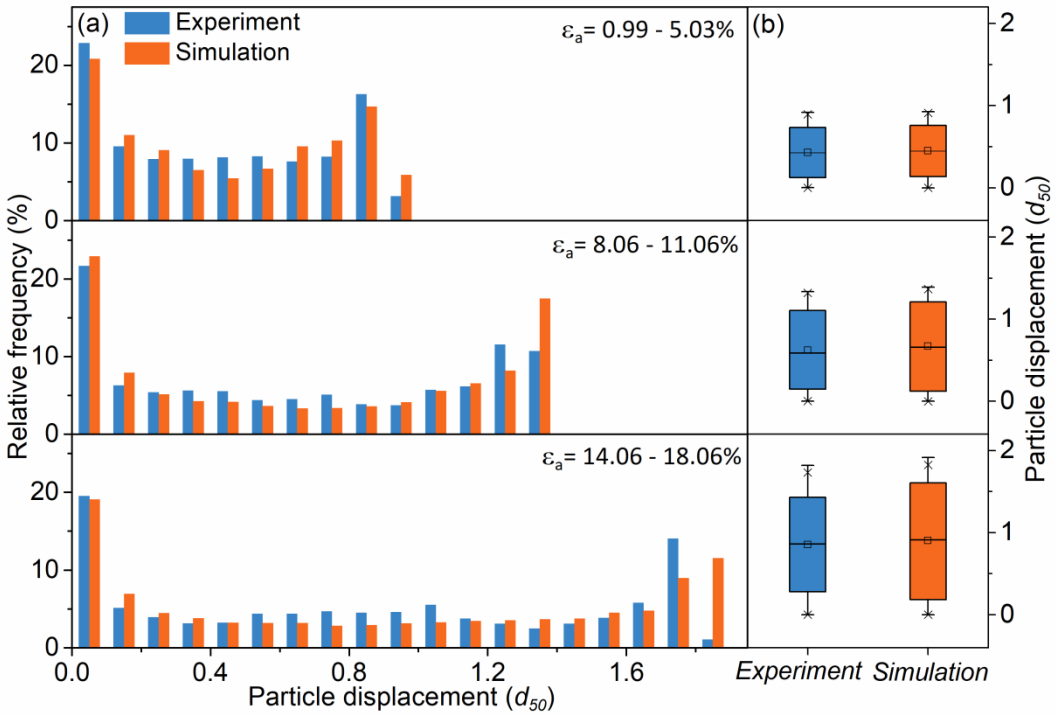

Fig. 10. (a) Frequency distributions and (b) box charts of incremental particle displacements during three axial strain increments for experiment test and FDEM simulation.

4.2 Microscopic dynamics

From the microscopic level, the sheared granular materials appear to strongly

rearrange themselves in response to shear. The varying local structure of particles leads to highly heterogeneous particle motion, as a result, granular materials deform in a nonaffine form [44]. The X-ray CT test and FDEM simulation allow us to quantify the nonaffine motion of particle using the local minimum nonaffine displacement $D^2_{\min}$, which measures the mean square deviation of the particle's position from the best-fit affine transformation of its neighborhood over the strain interval $\delta\varepsilon$ [60-62].

$$D^2_{\min}\left(\varepsilon, \varepsilon+\delta\varepsilon\right) = \frac{1}{N_i}\sum_{k}^{N_i}\left[\boldsymbol{\mu}_{ki}(\varepsilon+\delta\varepsilon) - \boldsymbol{\Lambda}_i(\varepsilon)\boldsymbol{\mu}_{ki}(\varepsilon)\right]^2 \tag{9}$$

where $\boldsymbol{\Lambda}_i\left(\varepsilon\right)$ is the best-fit affine deformation tensor of particle i extracted by minimizing the $D^2_{\min}\left(\varepsilon, \varepsilon+\delta\varepsilon\right)$ [63,64],

$$\boldsymbol{\Lambda}_i = \mathbf{X}\cdot\mathbf{Y}^{-1} \tag{10}$$

$$\mathbf{X} = \sum_{k}^{N_i}\boldsymbol{\mu}_{ki}(\varepsilon+\delta\varepsilon)\otimes\boldsymbol{\mu}_{ki}(\varepsilon) \tag{11}$$

$$\mathbf{Y} = \sum_{k}^{N_i}\boldsymbol{\mu}_{ki}(\varepsilon)\otimes\boldsymbol{\mu}_{ki}(\varepsilon) \tag{12}$$

$\boldsymbol{\mu}_{ki}\left(\varepsilon\right)$ is the displacement vector between reference particle i and its neighbor k at strain state ε. Note that the nonaffinity measure depends on the size of the neighborhood. Here, we take the cutoff distance as $1.5d_{50}$, which corresponds to the first minimum of the pair-correlation function $g\left(r\right)$ (Refer to Fig. 6a) [63]. The local strain tensor is deduced based on the affine tensor $\boldsymbol{\Lambda}$ by $\boldsymbol{\varepsilon}^L = -\left(\boldsymbol{\Lambda}+\boldsymbol{\Lambda}^T\right)/2$, we thus can calculate the local deviatoric strain $\varepsilon_q^L = \sqrt{\frac{2}{3}\boldsymbol{\varepsilon}^L_{dev}:\boldsymbol{\varepsilon}^L_{dev}}$ for each particle.

The nonaffine deformation $D^2_{\min}$ and local deviatoric strain ε_q^L are evaluated within the strain interval of $\Delta\varepsilon_a = 1.0\%$ at five loading states labelled in Fig.8. The

maps of ε_q^L shown in Fig. 11 display similar spatial distribution and temporal evolution for both X-ray micro-CT test and FDEM simulation. At 1.0% axial strain, we see only a few localized plastic zones randomly embedded in elastic deformation surroundings. After the onset of yielding, particles rearrange themselves to accommodate the increase of applied strain, a large number of activated plastic zones appeared as close-packed particles demarcate regions of high local strain magnitude. Eventually, those highly plastic zones are localized in a conjugate X-shaped band spanning the granular system. The annihilation and formation of those regions through cooperative particle motions is to sustain the applied shear. It turns out that the subsequent plastic activity is essentially dominated by the localized plastic region once the shear band formed, e.g., the evolution of this region through thickening and sliding. Although the evolution modes in experiment and simulation have so much in common, the thickness and spanning region of shear band is slightly different, which is probably due to the FDEM simulation lacks the consideration of multiscale contacting behavior of particles, where the FDEM contact model assumes the contact point is fully sticking before reaching the Column frictional resistance. For real particles with multi-scale structure characteristics, even slightest perturbation can drive the relative motion and affect the local rearrangement of particles due to the surface roughness of particles and friction on small length scales [5]. Furthermore, the discrepancy of variable friction conditions in particles is left unnoticed by adopting the same friction coefficient for all particles.

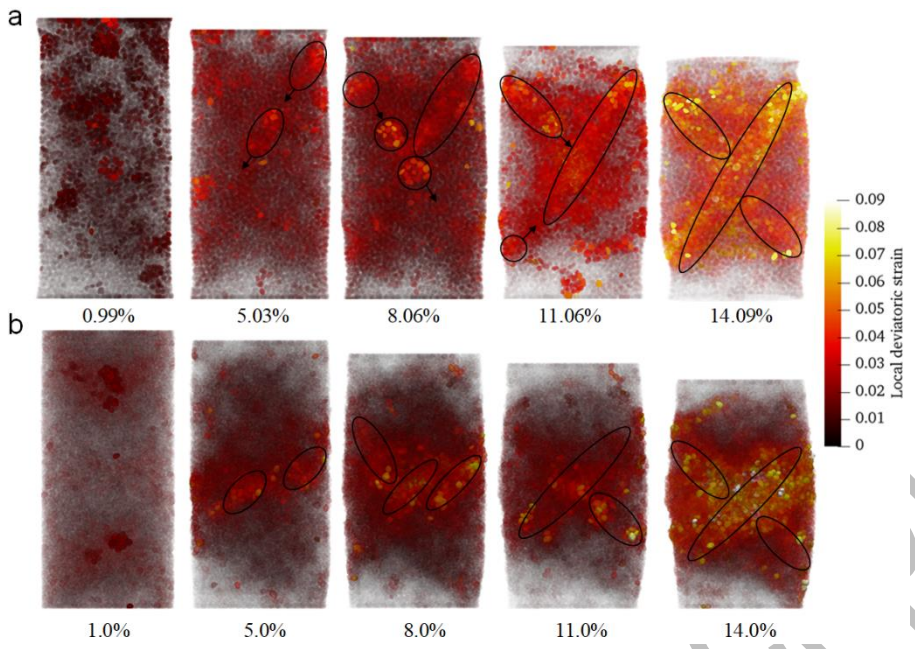

Fig. 11. The spatial distribution of local deviatoric strain at five strain states for both (a) experiment and (b) numerical simulation. The yellow and red particles indicate particle subjected to large local deviatoric strain, and particles with small ε_q^L are colored black and are transparent.

Fig. 12 presents the probability distribution functions (PDFs) of nonaffine displacements and local deviatoric strain at the loading states indicated in legend. Notably, the statistics of plastic heterogeneity exhibit remarkable consistency between the experiment and FDEM simulation. With the increase of ε_a, the large value part of the PDFs shift to right and the small part of the PDFs gradually lower, indicating the increased plastic heterogeneity during shearing. At the elastic regime, the granular system undergoes mainly elastic deformation, and few particles experience nonaffine displacements exceed $D_{\min}^2 = 0.01$. Thus, the sample deformation is relatively homogeneous at this state, which is consistent with the maps of ε_q^L at 1.0% axial strain shown in Fig. 11. After yielding, the population of larger $D_{\min}^2$ and ε_q^L increases, distorting the uniformity of deformation field and triggering other nearby shear transformation zones. Eventually, those plastic localized zones give rise to strain localization, manifesting as banded regions of intensive plastic deformation.

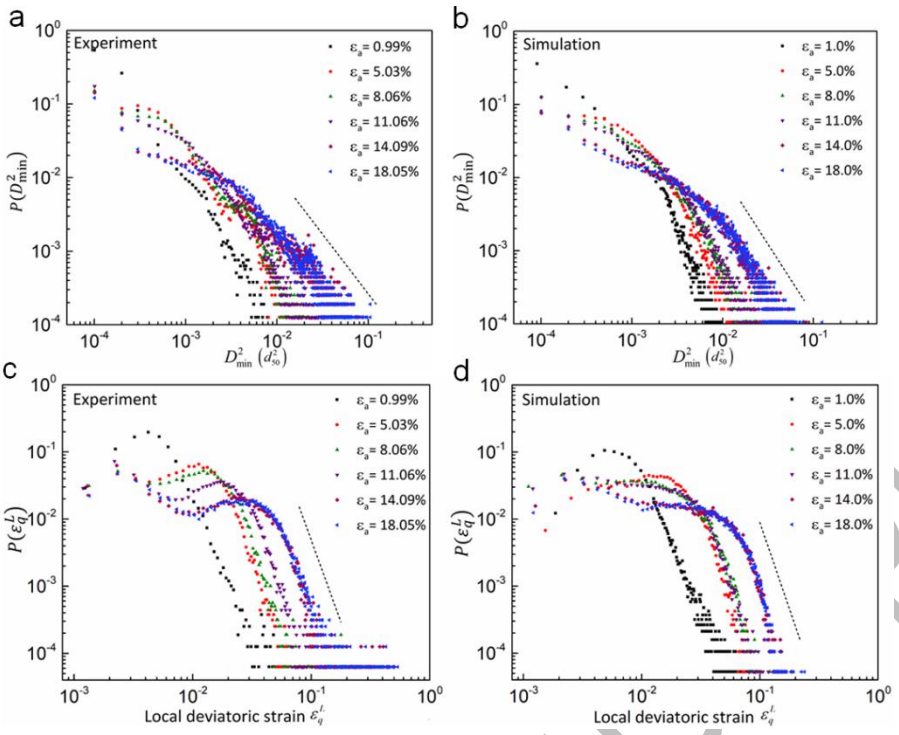

Fig. 12. Probability distribution functions of (a-b) nonaffine displacement $D^2_{\min}$ and (c-d) local deviatoric strain ε_q^L for experiment and simulation.

The power-law decay of $D^2_{\min}$ shown in Fig. 12a and b implies that particles with large nonaffine displacements are collectively organized. Those particles with similar nonaffine displacements tend to form compact clusters [65]. We then identify those activated nonaffine clusters by connecting the 10% highest $D^2_{\min}$ particles that are nearest neighbors. Fig. 13(a-b) show spatial distributions of the clusters of three loading states for experiment and simulation, respectively. The clusters are colored by the radius of gyration R_g :

$$R_g^2 = \frac{\sum_{i=1}^{N} V_i \left(\mathbf{r}_i - \bar{\mathbf{R}}\right)}{\sum_{i=1}^{N} V_i} \tag{13}$$

where the summation is over N particles belonging to the cluster, V_i and $\mathbf{r}_i$ is respectively the volume and position of particle i ,, $\bar{\mathbf{R}}$ is the center of mass of the cluster calculated by $\bar{\mathbf{R}} = \sum_{i=1}^{N} V_i \mathbf{r}_i \Big/ \sum_{i=1}^{N} V_i$.

At the initial elastic regime, the clusters are randomly distributed and predominantly isolated. With further strain, the clusters rearrange themselves by the change of their local topology, and some of the clusters are annihilated and others may proliferate by the merging of smaller clusters to form larger ones. When shearing to large strain, the nonaffine clusters accumulate along the direction of maximum shear stress, and forms an X-shaped shear band. Those findings suggest that these clusters are the fundamental plastic carrier and lead to the irreversible plastic deformation of the granular system.

Fig. 13(c) shows the cluster size distribution $P(s)$ for experiment and simulation covering strain states from 8.0% to 18.0%, where *s* is the number of particles in a cluster. The data is well fitted by a power law. The exponent is small for FDEM simulation, which indicates the particles with large nonaffine displacements are more inclined to clustering together. We think this difference is probably because the FDEM contact model assume the contact point is fully sticking before reaching the Column frictional resistance, whereas even slightest perturbation can drive the relative motion of particles due to the particle surface texture. Thus, it gives rise to more advanced contact model in future numerical simulation method. As shown in Fig. 13d, the gyration radius shows power-law growth with the cluster size, i.e., $R_g \propto s^{1/\mathrm{d}_f}$. The clusters of both experiment and simulation have a fractal dimension d_f of approximate 2.0. Similar fractal clusters have been observed for the fast translating clusters in cyclic sheared granular systems [63].

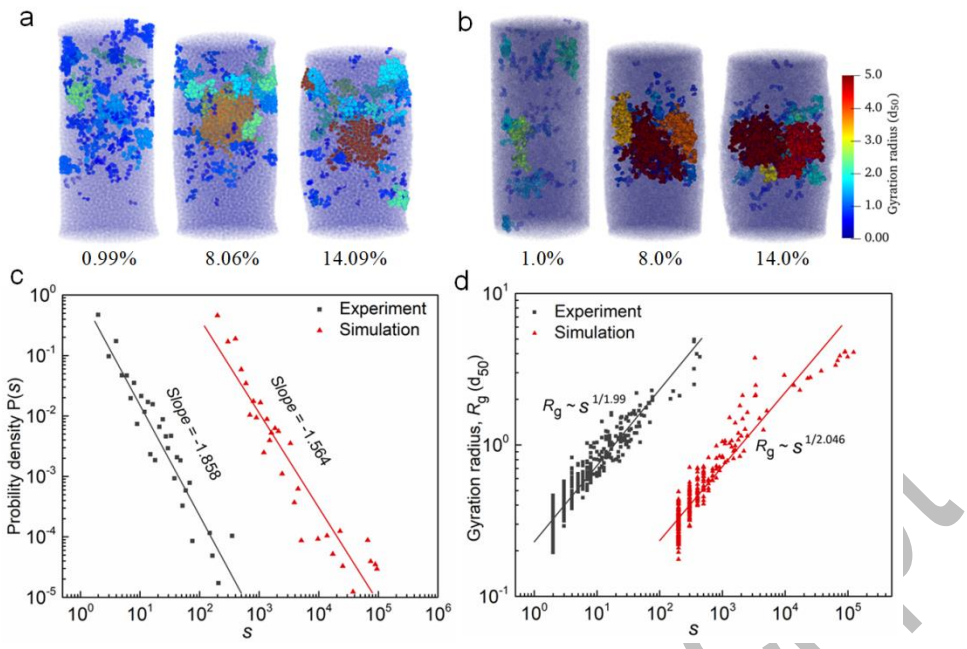

Fig. 13. (a-b) Spatial distributions of the clusters at axial strain 0.99%, 8.06%, and 14.09% for experiment and simulation respectively. Particles of a cluster are colored according to the cluster gyration radius, other particles are made transparent for clarity. (c) Cluster size distributions. (d) Radius of gyration of the clusters versus the cluster size. Data for simulation are shifted horizontally by 10^2 for clarity. The solid lines are power-law fits to the data.

5. Contact force network

We have seen a rather satisfactory agreement of the macroscopic properties, as well as the local ones, between the X-ray micro-CT test and FDEM simulation. The comparison of distribution of contact normal vector between experiment and simulation is shown in Fig.14. It is seen that there is a good agreement at the distributions and evolutions of inter-particle contact information between experiment and FDEM simulation along the whole shearing process. A slight difference of magnitude in local corner branch is attributed to a possible over-estimation of inter-particle contacts. That is, a global threshold is applied to the image segmentation, which may result in the over-detection of inter-particle contacts because of the partial volume effect related to imaging resolution. Overall, we see that the slight over-estimation of the inter-particle contacts does not have a significant influence on

the overall contact behavior. Here, we probe the contact force evolution accessible to numerical simulation. The angular distributions of the normal contact forces between particles are shown in Fig.15a, where the length and color represent the density of normal contact vector and the average normal contact forces oriented within the angles, respectively. It clearly shows that the normal contact force distributes isotropically prior to shearing and becomes much more anisotropic as a preferred orientation towards the vertical direction showing up and remain this way through the post-peak loading process. The contacts aligned with the loading direction transmit markedly larger contact forces, thereby, the granular system strengthens its capability to resist the vertical load.

The relatively dominant bias along loading direction of the normal contact forces manifesting strong force chains plotted in Fig.15 (b-c), where the chains are scaled in thickness, color and opacity by being proportional to the magnitude of contact forces. It is notable that the spatial and temporal evolutions of the force chains are shown from different perspectives as approximately parallel to the X and Y axes, respectively. Initially, the intra-particle force exhibits an isotropic distribution with a small magnitude, but strong force chains form along the loading direction at the peak stress state, which is representative of force transmission patterns. However, as the shear strain increase, the force chain network becomes sparse and scatter because of dilation, and the network is more vulnerable to collapse when the shear bands have completely formed, which is most apparent at 14.0% axial strains. More particles begin to lose the capacity of sustaining force transmission manifesting the enlarged local voids located inside the force chain network (marked by red dotted circles). The collapse coinciding with shear band formation is readily comprehensible because of the large induced structural voids induced by more floating particles (involving few contacts) formation

within the shear bands.

Further insights into the quantitative linkage between particle stress dynamics and nonaffine behavior. Here, the particle stress is calculated as $q=\sqrt{\frac{1}{2}\sigma_{ij}^{'}\sigma_{ij}^{'}}$, where $\sigma_{ij}^{'}$ is the deviatoric part of the particle stress tensor σ_{ij}. Specifically, we quantify the temporal fluctuations of particle stress in terms of the volatility in the Black-Scholes model [7][66]. For each particle, the particle stress is regarded as a discretized series q_i, where i corresponds to a strain state, the instantaneous 'return' is defined as:

$$R_i=\ln\left(q_i/q_{i-1}\right) \tag{14}$$

The volatility of the particle stress data series is quantified by the standard deviation of R:

$$V=\sqrt{\frac{1}{N-1}\sum_{i=1}^{N}\left(R_i-\bar{R}\right)^2} \tag{15}$$

where N is the number of strain intervals in the particle stress data set, for our study, the particle stress is extracted at the strain interval $\Delta\varepsilon_a=2.5\times10^{-3}$ during a strain window $\varepsilon_a=10\%:\ 20\%$.

Fig. 16 correlate the volatility of particle stress V with the nonaffine behavior, as measured by $D_{\min}^2$. As the data indicates, particles with large stress volatility exhibit more intensive nonaffine motions. There is a strong correlation between the particle stress volatility and nonaffine displacement with a correlation coefficient of 0.541, and the correlation is significant at the 0.01 level. The result quantitatively demonstrates a deep correlation between particle stress fluctuations and particle plastic rearrangement.

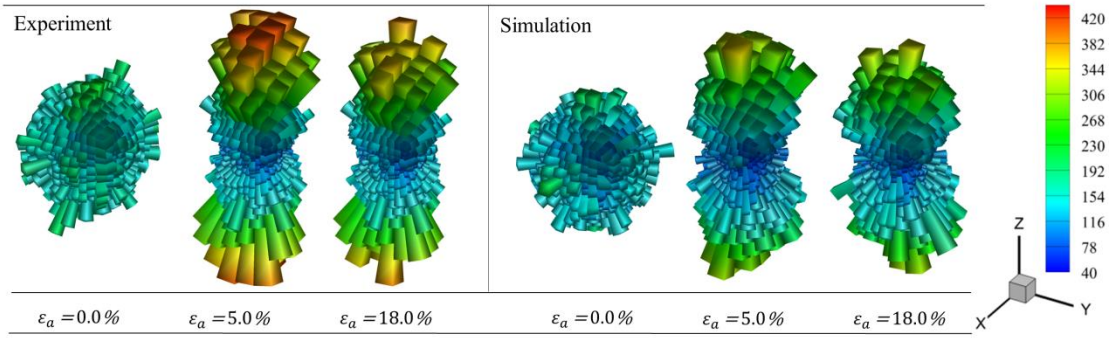

Fig. 14. Angular distribution of contact normal vector at three strain states, initial state, peak state and critical state, for both experiment and numerical simulation, the length and color of each corner indicate the density of branch vector and contact normal vector oriented within the angles, respectively.

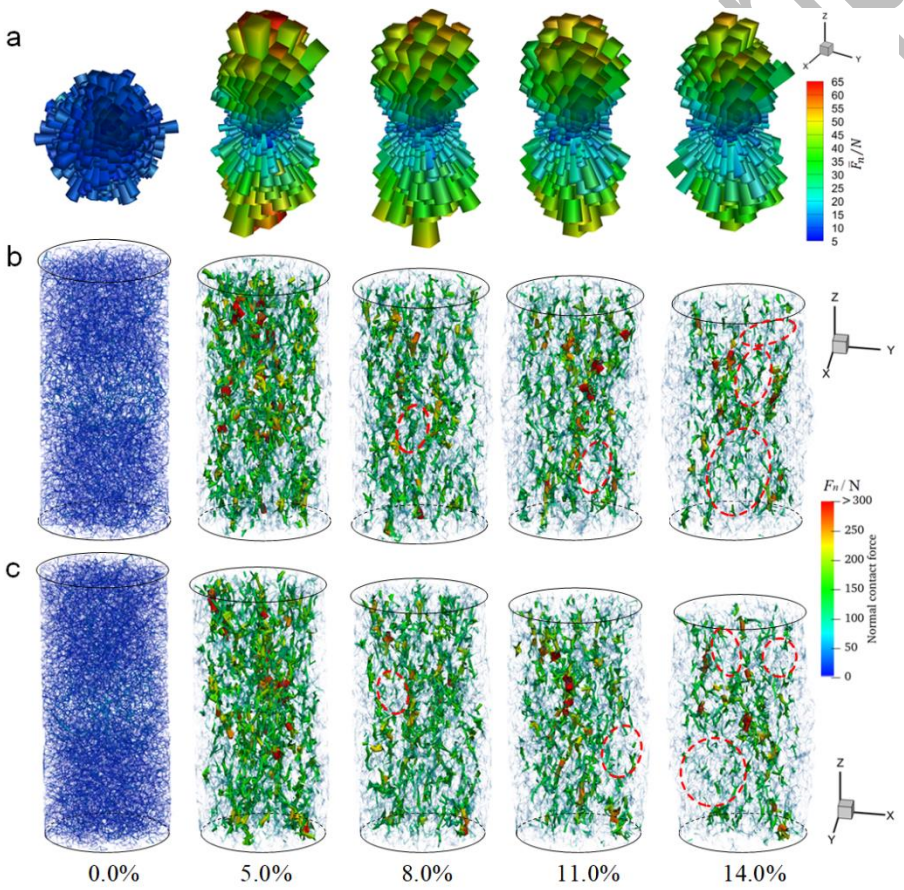

Fig. 15. (a) Rose diagrams of the normal contact force at different strain states. The length and color represent the density of normal contact vector and the average normal contact forces oriented within the angles, respectively. (b-c) Spatial distributions of force chains at different strain states from different perspectives as approximately parallel to the X and Y axes, respectively. The thickness, color and opacity of the chain are proportional to the magnitude of contact forces.

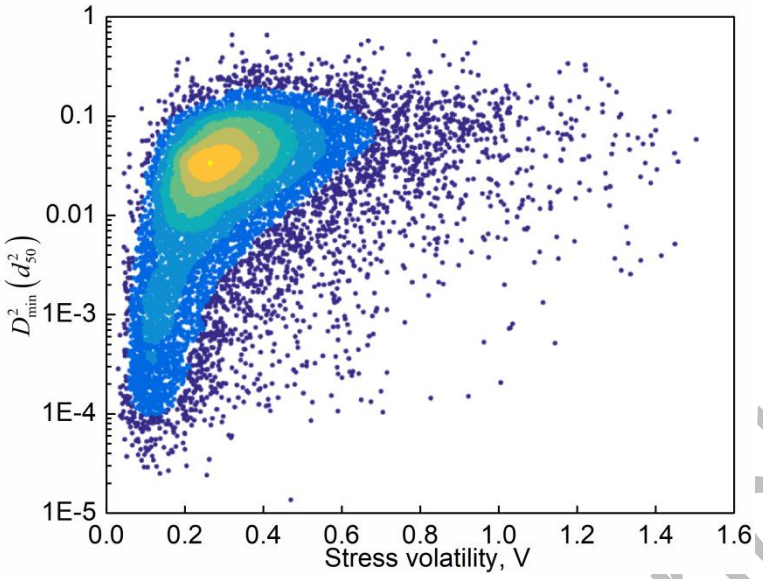

Fig. 16. Correlations between particle nonaffine displacements $D^2_{\min}$ and particle stress volatility V. The color represents the data point density in range (0, 1) and the yellow represents the higher density.

6. Conclusions

In this work, we propose an enhanced tool to investigate the mechanical behavior of granular materials by combining the merits of the in-situ X-ray CT test and FDEM modeling. We then perform spherical harmonic analysis to characterize and reconstruct the multiscale morphological characteristics of irregularly shaped particles. A set of the SH rotation-invariants of each particle are used as matching index in the particle tracking. The implemented particle tracking algorithm enables accurate matching of particles even at the large strain interval. Rely on the detailed spherical harmonic reconstruction, we implement the conversion from X-ray image data into FDEM numerical sample with the consistent particle morphology and disordered structure.

Without calibrating FDEM parameters based on experiment test, the FDEM simulation results quantitatively agree with the overall response recorded in experiment test. Moreover, the particle scale dynamics including the nonaffine

particle displacements and particle clustering behavior, show a remarkable quantitative agreement between simulation and experiment. It provides a clear understanding in two aspects: the particle tracking is robust and accurate; the FDEM modeling of granular materials is complete at both macro scale and micro scale. The slight difference between X-ray CT test and FDEM simulation may due to the lack of consideration of the multiscale contact behavior in FDEM contact model. The localized triggering of large nonaffine particle displacements is responsible for the plastic deformation, highlighting a spatial heterogeneity of dynamics behavior. The spatiotemporal evolution of such localized zones controls the macroscopic responses of the system. We further probe the contact force network via FDEM simulation. The spatially heterogeneous dynamics induce the evolution of contact force network, and especially the collapse of contact force chain networks coincide with the shear band formation. The collapse is relevant to the large induced structural voids formation within the shear transformation zones. Finally, we find the particle plastic rearrangements are closely related to the particle stress fluctuations.

To conclude, the proposed tool, combining experimental X-ray CT and numerical FDEM, sheds new light on bridging length scales from particle size to granular system, making accurately understanding physical mechanism of granular system failure simple and flexible. Further, the enhanced tool makes it possibilities in studying the microscopic behavior of granular systems considering the particle breakage, and the complex dynamics over very small time scales because of the high temporal resolution in FDEM simulation.

Acknowledgments

The authors thank Ms. Yu Wang and Dr. Aly Abdelaziz from University of Toronto for help in executing the experiments. This work was supported by the National

Natural Science Foundation of China (Grant No. 51825905, U1865204, and 51779194) and Science project of China Huaneng Group Co. Ltd (HNKJ18-H26). The numerical calculations in this work have been done on the supercomputing system in the Supercomputing Center of Wuhan University.

Appendix A Efficiency of SH-invariants to track particles

The number of individual particles at the first and second scans is 15961 and 15952, respectively, within which 15927 particles are tracked and 34 particles are lost during in the first strain interval. Fig. A1 shows the relative deviation $ERR = (\chi_d - \chi_r)/\chi_r$ of particle shapes for reference particle (χ_r) and matching particle (χ_d) between adjacent loading states, where the deviation is basically within 4.0%. As shown in Table A1, all particle pairs are divided into four groups according to the magnitudes of particle volume difference, aspect ratio difference and sphericity difference. The first row in the table represents the shape difference, and the second row represents the number of particle pairs located in each group. The particle pair with smaller differences in morphology features are normally has a higher possibility to be correctly matched. We select reference particles and corresponding matching particles located in the group of 2.0%-10.0%, and an imaging comparison is made to check the matching result. Only six particle pairs are incorrectly matched, which indicates the matching provides highly accurate matching results in almost all the cases. For several error matched particles, it may be due to the information loss, or a significant image segmentation error occurs. As shown in Fig. A2, several image segmentation errors, such as over-segmentation (Fig. A2(a)) and under-segmentation (Fig. A2(b-c)), occur among the six particles which result in incorrect matching.

In the future, high-resolution X-ray CT data and requisite image processing are needed to capture enough information in the higher frequency components to improve the matching precision. Those extensions would be better suited for matching irregularly shaped objects.

Table A1 Results of the matching

0-0.5%	0.5%-2.0%	2.0%-5.0%	2.0%-10.0%
9322	6102	459	28

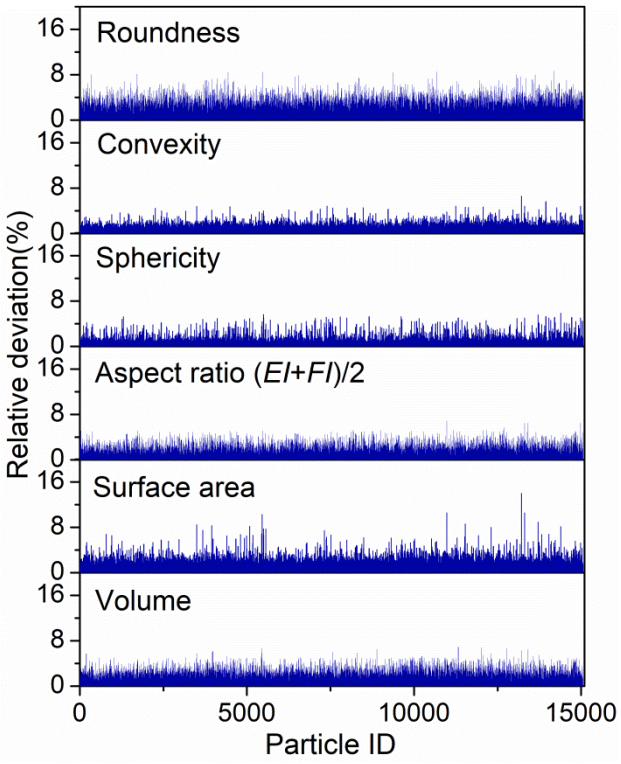

Fig. A1. The relative deviation of particle shapes for reference particle and matching particle between adjacent loading states.

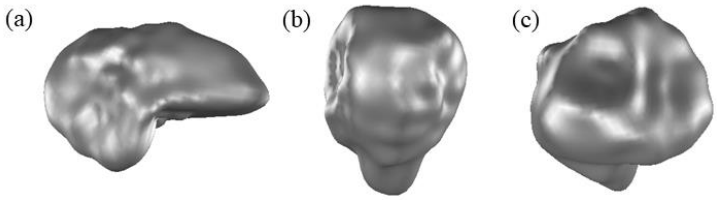

Fig. A2. Image segmentation errors (a) over-segmentation (b-c) under-segmentation.

References

[1] Majmudar, T. S., & Behringer, R. P. (2005). Contact force measurements and stress-induced anisotropy in granular materials. Nature, 435(7045), 1079. https://doi.org/10.1038/nature03805.

[2] Andò, E., Hall, S. A., Viggiani, G., Desrues, J., & Bésuelle, P. (2012). Grain-scale experimental investigation of localised deformation in sand: a discrete particle tracking approach. Acta Geotechnica, 7(1), 1-13. https://doi.org/10.1007/s11440-011-0151-6.

[3] Xia, C., Li, J., Cao, Y., Kou, B., Xiao, X., Fezzaa, K., ... & Wang, Y. (2015). The structural origin of the hard-sphere glass transition in granular packing. Nature communications, 6, 8409. doi:10.1038/ncomms9409.

[4] Weis, S., & Schröter, M. (2017). Analyzing X-ray tomographies of granular packings. Review of Scientific Instruments, 88(5), 051809.

https://doi.org/10.1063/1.4983051.
[5] Kou, B., Cao, Y., Li, J., Xia, C., Li, Z., Dong, H., ... & Wang, Y. (2017). Granular materials flow like complex fluids. Nature, 551(7680), 360. https://doi.org/10.1038/nature24062.
[6] Zhao, Q., Tisato, N., Kovaleva, O., & Grasselli, G. (2018). Direct Observation of Faulting by Means of Rotary Shear Tests Under X-Ray Micro-Computed Tomography. Journal of Geophysical Research: Solid Earth, 123(9), 7389-7403. https://doi.org/10.1029/2017JB015394.
[7] Murphy, K. A., Dahmen, K. A., & Jaeger, H. M. (2019). Transforming Mesoscale Granular Plasticity Through Particle Shape. Physical Review X, 9(1), 011014. DOI: 10.1103/PhysRevX.9.011014.
[8] Alshibli, K., Cil, M. B., Kenesei, P., & Lienert, U. (2013). Strain tensor determination of compressed individual silica sand particles using high-energy synchrotron diffraction. Granular matter, 15(5), 517-530. https://doi.org/10.1007/s10035-013-0424-x.
[9] Hurley, R. C., Herbold, E. B., & Pagan, D. C. (2018). Characterization of the crystal structure, kinematics, stresses and rotations in angular granular quartz during compaction. Journal of Applied Crystallography, 51(4). https://doi.org/10.1107/S1600576718006957.
[10] Karatza, Z., Andò, E., Papanicolopulos, S. A., Ooi, J. Y., & Viggiani, G. (2017). Evolution of deformation and breakage in sand studied using X-ray tomography. Géotechnique, 68(2), 107-117. https://doi.org/10.1680/jgeot.16.P.208.
[11] Guillard, F., Marks, B., & Einav, I. (2017). Dynamic X-ray radiography reveals particle size and shape orientation fields during granular flow. Scientific reports, 7(1), 8155. DOI:10.1038/s41598-017-08573-y.
[12] Wiebicke, M., Andò, E., Herle, I., & Viggiani, G. (2017). On the metrology of interparticle contacts in sand from x-ray tomography images. Measurement Science and Technology, 28(12), 124007. doi:10.1088/1361-6501/aa8dbf.
[13] Afshar, T., Disfani, M. M., Narsilio, G. A., & Arulrajah, A. (2018). Post-breakage changes in particle properties using synchrotron tomography. Powder Technology, 325, 530-544. https://doi.org/10.1016/j.powtec.2017.11.039.
[14] Cheng, Z., & Wang, J. (2018). A particle-tracking method for experimental investigation of kinematics of sand particles under triaxial compression. Powder technology, 328, 436-451. https://doi.org/10.1016/j.powtec.2017.12.071.
[15] Cheng, Z., & Wang, J. (2018). Experimental investigation of inter-particle contact evolution of sheared granular materials using X-ray micro-tomography. Soils and Foundations, 58(6), 1492-1510. https://doi.org/10.1016/j.sandf.2018.08.008.
[16] Kong, D., & Fonseca, J. (2019). On the kinematics of shelly carbonate sand using X-ray micro tomography. Engineering Geology, 261, 105268. https://doi.org/10.1016/j.enggeo.2019.105268.
[17] Chevalier, B., Tsutsumi, Y., & Otani, J. (2019). Direct shear behavior of a mixture of sand and tire chips using X-ray computed tomography and discrete element method. International Journal of Geosynthetics and Ground Engineering, 5(2), 7. https://doi.org/10.1007/s40891-019-0160-3.
[18] Druckrey, A. M., & Alshibli, K. A. (2014). 3D behavior of sand particles using X-ray synchrotron micro-tomography. In Geo-Congress 2014: Geo-characterization and Modeling for Sustainability (pp. 2814-2821).
[19] Garboczi, E. J. (2002). Three-dimensional mathematical analysis of particle shape using X-ray tomography and spherical harmonics: Application to aggregates used in concrete. Cement and concrete research, 32(10), 1621-1638. https://doi.org/10.1016/S0008-8846(02)00836-0.
[20] Shen, L., Farid, H., & McPeek, M. A. (2009). Modeling three-dimensional morphological structures using spherical harmonics. Evolution: International Journal of Organic Evolution, 63(4), 1003-1016. https://doi.org/10.1111/j.1558-5646.2008.00557.x.
[21] Zhou, B., Wang, J., & Zhao, B. (2015). Micromorphology characterization and reconstruction of sand particles using micro X-ray tomography and spherical harmonics. Engineering geology, 184, 126-137. https://doi.org/10.1016/j.enggeo.2014.11.009.
[22] Wei, D., Wang, J., & Zhao, B. (2018). A simple method for particle shape generation with spherical harmonics. Powder technology, 330, 284-291. https://doi.org/10.1016/j.powtec.2018.02.006.

[23] Kazhdan, M., Funkhouser, T., & Rusinkiewicz, S. (2003, June). Rotation invariant spherical harmonic representation of 3 d shape descriptors. In Symposium on geometry processing(Vol. 6, pp. 156-164).
[24] Zhao, B. D., Wei, D. H., & Wang, J. F. (2017). Particle shape quantification using rotation-invariant spherical harmonic analysis. Géotechnique Letters, 7(2), 190-196. http://dx.doi.org/10.1680/jgele.17.00011.
[25] Zhou, B., Wang, J., & Wang, H. (2018). A novel particle tracking method for granular sands based on spherical harmonic rotational invariants. Géotechnique, 68(12), 1116-1123. DOI: 10.1680/jgeot.17.t.040.
[26] Saadatfar, M., Sheppard, A. P., Senden, T. J., & Kabla, A. J. (2012). Mapping forces in a 3D elastic assembly of grains. Journal of the Mechanics and Physics of Solids, 60(1), 55-66. https://doi.org/10.1016/j.jmps.2011.10.001.
[27] Andrade, J. E., & Avila, C. F. (2012). Granular element method (GEM): linking inter-particle forces with macroscopic loading. Granular Matter, 14(1), 51-61. https://doi.org/10.1007/s10035-011-0298-8.
[28] Hurley, R., Marteau, E., Ravichandran, G., & Andrade, J. E. (2014). Extracting inter-particle forces in opaque granular materials: beyond photoelasticity. Journal of the Mechanics and Physics of Solids, 63, 154-166. https://doi.org/10.1016/j.jmps.2013.09.013.
[29] Hurley, R. C., Hall, S. A., Andrade, J. E., & Wright, J. (2016). Quantifying interparticle forces and heterogeneity in 3D granular materials. Physical review letters, 117(9), 098005. https://doi.org/10.1103/PhysRevLett.117.098005.
[30] Hurley, R. C., Lim, K. W., Ravichandran, G., & Andrade, J. E. (2016b). Dynamic inter-particle force inference in granular materials: method and application. Experimental Mechanics, 56(2), 217-229. https://doi.org/10.1007/s11340-015-0063-8.
[31] Hurley, R. C., Hall, S. A., & Wright, J. P. (2017). Multi-scale mechanics of granular solids from grain-resolved X-ray measurements. Proceedings of the Royal Society A: Mathematical, Physical and Engineering Sciences, 473(2207), 20170491. https://doi.org/10.1098/rspa.2017.0491.
[32] Hurley, R. C., Lind, J., Pagan, D. C., Akin, M. C., & Herbold, E. B. (2018b). In situ grain fracture mechanics during uniaxial compaction of granular solids. Journal of the Mechanics and Physics of Solids, 112, 273-290. https://doi.org/10.1016/j.jmps.2017.12.007.
[33] Zhai, C., Herbold, E. B., Hall, S. A., & Hurley, R. C. (2019). Particle rotations and energy dissipation during mechanical compression of granular materials. Journal of the Mechanics and Physics of Solids, 129, 19-38. DOI: 10.1016/j.jmps.2019.04.018.
[34] Liu, J., Zhou, W., Ma, G., Yang, S., & Chang, X. (2020a). Strong contacts, connectivity and fabric anisotropy in granular materials: A 3D perspective. Powder Technology. doi:10.1016/j.powtec.2020.03.018.
[35] Liu, J., Wautier, A., Bonelli, S., Nicot, F., & Darve, F. (2020b). Macroscopic softening in granular materials from a mesoscale perspective. International Journal of Solids and Structures, 193, 222-238.
[36] Alshibli, K. A., Jarrar, M. F., Druckrey, A. M., & Al-Raoush, R. I. (2016). Influence of particle morphology on 3D kinematic behavior and strain localization of sheared sand. Journal of Geotechnical and Geoenvironmental Engineering, 143(2), 04016097. DOI: 10.1061/(ASCE)GT.1943-5606.0001601.
[37] Ma, G., Zhou, W., & Chang, X. L. (2014). Modeling the particle breakage of rockfill materials with the cohesive crack model. Computers and Geotechnics, 61, 1320–1143. https://doi.org/10.1016/j.compgeo.2014.05.006.
[38] Ma, G., Zhou, W., Chang, X.-L., & Chen, M.-X. (2016a). A hybrid approach for modeling of breakable granular materials using combined finite-discrete element method. Granular Matter, 18(1), 7. https://doi.org/10.1007/s10035-016-0615-3.
[39] Nadimi, S., & Fonseca, J. (2018). A micro finite-element model for soil behaviour: numerical validation. Géotechnique, 68(4), 364–369. doi:10.1680/jgeot.16.p.163Oda, M. (1982). Fabric tensor for discontinuous geological materials. Soils and Foundations, 22(4), 96-108. https://doi.org/10.3208/sandf1972.22.4_96.
[40] Kawamoto, R., Andò, E., Viggiani, G., & Andrade, J. E. (2016). Level set discrete element method for three-dimensional computations with triaxial case study. Journal of the Mechanics and Physics of Solids, 91, 1-13. https://doi.org/10.1016/j.jmps.2016.02.021.

[41] Kawamoto, R., Andò, E., Viggiani, G., & Andrade, J. E. (2018). All you need is shape: Predicting shear banding in sand with LS-DEM. Journal of the Mechanics and Physics of Solids, 111, 375-392. https://doi.org/10.1016/j.jmps.2017.10.003.
[42] Ma, G., Zhou, W., Chang, X., Ng, T.-T., & Yang, L. (2016). Formation of shear bands in crushable and irregularly shaped granular materials and the associated microstructural evolution. Powder Technology, 301, 118–130. https://doi.org/10.1016/j.powtec.2016.05.068.
[43] Ma, G., Zhou, W., Regueiro, R. A., Wang, Q., & Chang, X. (2017). Modeling the fragmentation of rock grains using computed tomography and combined FDEM. Powder technology, 308, 388-397. https://doi.org/10.1016/j.powtec.2016.11.046.
[44] Ma, G., Regueiro, R. A., Zhou, W., Wang, Q., & Liu, J. (2018). Role of particle crushing on particle kinematics and shear banding in granular materials. Acta Geotechnica, 13(3), 601–618. https://doi.org/10.1007/s11440-017-0621-6.
[45] Ma, G., Regueiro, R. A., Zhou, W., & Liu, J. (2019). Spatiotemporal analysis of strain localization in dense granular materials. Acta Geotechnica, 14(4), 973-990. https://doi.org/10.1007/s11440-018-0685-y.
[46] Ma, G., Chen, Y., Yao, F., Zhou, W., & Wang, Q. (2019). Evolution of particle size and shape towards a steady state: Insights from FDEM simulations of crushable granular materials. Computers and Geotechnics, 112, 147-158. https://doi.org/10.1016/j.compgeo.2019.04.022.
[47] Druckrey, A. M., & Alshibli, K. A. (2016). 3D finite element modeling of sand particle fracture based on in situ X-Ray synchrotron imaging. International Journal for Numerical and Analytical Methods in Geomechanics, 40(1), 105-116. https://doi.org/10.1002/nag.2396.
[48] Imseeh, W. H., & Alshibli, K. A. (2018). 3D finite element modelling of force transmission and particle fracture of sand. Computers and Geotechnics, 94, 184-195. https://doi.org/10.1016/j.compgeo.2017.09.008.
[49] Wei, D., Zhao, B., Dias-da-Costa, D., & Gan, Y. (2019). An FDEM study of particle breakage under rotational point loading. Engineering Fracture Mechanics, 212, 221-237. https://doi.org/10.1016/j.engfracmech.2019.03.036.
[50] Zhao, Q., Tisato, N., & Grasselli, G. (2017). Rotary shear experiments under X-ray micro-computed tomography. Review of Scientific Instruments, 88(1), 015110. https://doi.org/10.1063/1.4974149.
[51] Tisato, N., Zhao, Q., & Grasselli, G. (2016). Experimental rock physics under micro-CT. In SEG Technical Program Expanded Abstracts 2016 (pp. 3251-3255). Society of Exploration Geophysicists. https://doi.org/10.1190/segam2016-13949603.1.
[52] Imseeh, W. H., Druckrey, A. M., & Alshibli, K. A. (2018). 3D experimental quantification of fabric and fabric evolution of sheared granular materials using synchrotron micro-computed tomography. Granular Matter, 20(2), 24. https://doi.org/10.1007/s10035-018-0798-x.
[53] Wählby, C., Sintorn, I. M., Erlandsson, F., Borgefors, G., & Bengtsson, E. (2004). Combining intensity, edge and shape information for 2D and 3D segmentation of cell nuclei in tissue sections. Journal of microscopy, 215(1), 67-76. https://doi.org/10.1111/j.0022-2720.2004.01338.x.
[54] Zhao, B., Wang, J., Coop, M. R., Viggiani, G., & JIANG, M. (2015). An investigation of single sand particle fracture using X-ray micro-tomography. Géotechnique, 65(8), 625–641. doi:10.1680/geot.4.p.157
[55] Alam, M., Haque, A., & Ranjith, P. (2018). A study of the particle-level fabric and morphology of granular soils under one-dimensional compression using insitu X-ray CT imaging. Materials, 11(6), 919. https://doi.org/10.3390/ma11060919.
[56] Mathworks (2016) MATLAB, Version R2016a.
[57] Wei, D., Wang, J., Nie, J., & Zhou, B. (2018b). Generation of realistic sand particles with fractal nature using an improved spherical harmonic analysis. Computers and Geotechnics, 104, 1-12. https://doi.org/10.1016/j.compgeo.2018.08.002.
[58] Erdoğan, S. T., Forster, A. M., Stutzman, P. E., & Garboczi, E. J. (2017). Particle-based characterization of Ottawa sand: Shape, size, mineralogy, and elastic moduli. Cement and Concrete Composites, 83, 36–44. doi:10.1016/j.cemconcomp.2017.07.003.
[59] Yang, L., Wang, D., Guo, Y., & Liu, S. (2016). Tribological behaviors of quartz sand particles for hydraulic fracturing. Tribology International, 102, 485-496. https://doi.org/10.1016/j.triboint.2016.06.017.

[60] Falk, M. L., & Langer, J. S. (1998). Dynamics of viscoplastic deformation in amorphous solids. Physical Review E, 57(6), 7192. https://doi.org/10.1103/PhysRevE.57.7192.
[61] Ding, J., Patinet, S., Falk, M. L., Cheng, Y., & Ma, E. (2014). Soft spots and their structural signature in a metallic glass. Proceedings of the National Academy of Sciences, 111(39), 14052-14056. https://doi.org/10.1073/pnas.1412095111.
[62] Cubuk, E. D., Ivancic, R. J. S., Schoenholz, S. S., Strickland, D. J., Basu, A., Davidson, Z. S., ... & Keim, N. C. (2017). Structure-property relationships from universal signatures of plasticity in disordered solids. Science, 358(6366), 1033-1037. DOI: 10.1126/science.aai8830.
[63] Chikkadi, V., & Schall, P. (2012). Nonaffine measures of particle displacements in sheared colloidal glasses. Physical Review E, 85(3), 031402. https://doi.org/10.1103/PhysRevE.85.031402.
[64] Guo, N., & Zhao, J. (2014). Local fluctuations and spatial correlations in granular flows under constant-volume quasistatic shear. Physical Review E, 89(4), 042208. https://doi.org/10.1103/PhysRevE.89.042208.
[65] Kou, B., Cao, Y., Li, J., Xia, C., Li, Z., Dong, H., ... & Wang, Y. (2018). Translational and rotational dynamical heterogeneities in granular systems. Physical review letters, 121(1), 018002. DOI: 10.1103/PhysRevLett.121.018002.
[66] Adams, D. Bloomfield, P. Booth, and P. England, Investment Mathematics and Statistics (Graham & Trotman, London, United Kingdom, 1993).
[67] Wu, M., Wang, J., Russell, A., & Cheng, Z. (2020). DEM modelling of mini-triaxial test based on one-to-one mapping of sand particles. Géotechnique, 1-14.
[68] Druckrey, A. M., Alshibli, K. A., & Al-Raoush, R. I. (2016). 3D characterization of sand particle-to-particle contact and morphology. Computers and Geotechnics, 74, 26-35.
[69] Tatone, B. S., & Grasselli, G. (2015). A calibration procedure for two-dimensional laboratory-scale hybrid finite–discrete element simulations. International Journal of Rock Mechanics and Mining Sciences, 75, 56-72.